American Mineralogist, Volume 93, pages 1034–1042, 2008

Ramanite-(Cs) and ramanite-(Rb): New cesium and rubidium pentaborate tetrahydrate minerals identified with Raman spectroscopy

RAINER THOMAS,[1,*] PAUL DAVIDSON,[2] AND ANDREAS HAHN[1]

[1]GeoForschungsZentrum Potsdam, Telegrafenberg B120, D-14473 Potsdam, Germany
[2]ARC Centre of Excellence in Ore Deposits, University of Tasmania, Hobart 7001, Australia

ABSTRACT

This study of melt and fluid inclusions in graphic pegmatite quartz from the Island of Elba, Italy has identified silicate melts and coexisting aqueous fluid from the final stage of pegmatite formation, which contain extremely high concentrations of boron (up to 19.8 mass% B_2O_3), cesium (>5 mass% Cs_2O), and rubidium (>0.5 mass% Rb_2O). Several boron-bearing minerals have been identified in melt and fluid inclusions, including sassolite (H_3BO_3) and santite ($KB_5O_8{\cdot}4H_2O$). In addition, we have found two new minerals observed as daughter mineral phases, and these have been accepted by the IMA, Commission on New Minerals, Nomenclature and Classification (CNMNC) as ramanite-(Cs) (2007-007), monoclinic β-cesium pentaborate tetrahydrate ($CsB_5O_8{\cdot}4H_2O$) with space group *C*2/*c*, and ramanite-(Rb) (2007-006), orthorhombic rubidium pentaborate tetrahydrate ($RbB_5O_8{\cdot}4H_2O$) with space group *Aba*2.

At the moment, given sample constraints, we cannot directly determine some of the properties traditionally reported for new minerals; however, both phases have Raman spectra identical to spectra obtained on synthetic Cs and Rb pentaborates, which were studied for comparison. Although difficult to recognize optically, ramanite-(Cs) and ramanite-(Rb) have distinctive Raman spectra allowing simple and definitive identification from other translucent phases found in many hypersaline fluid inclusions. Although currently only identified from a limited number of occurrences, given the availability of a definitive means of identification, we suspect that ramanite-(Rb) and ramanite-(Cs) may in fact be common, at least in boron-rich pegmatites.

Keywords: Fluid and melt inclusions, strong enrichment of boron, rubidium, and cesium, Raman spectroscopy, new Cs and Rb minerals, ramanite-(Cs), ramanite-(Rb)

INTRODUCTION

During the study of melt and fluid inclusions in a pegmatite sample from the Island of Elba, we found two types of melt inclusions (called type-A and type-B), which represent trapping of a pair of conjugate melts resulting from the immiscible separation of an original volatile-rich silicate melt (Thomas et al. 2006c). The type-A melt inclusions are very small (about 5 μm in diameter) and could not be analyzed by electron microprobe. Co-genetic near-critical type-B melt inclusions are larger (~50 μm in diameter), resemble fluid inclusions at room temperature (Figs. 1a and 1b), and when experimentally re-homogenized (Figs. 1c and 1d) gave high concentrations of Cs by microprobe. Boron is present in such inclusions as generally tabular daughter crystals of sassolite (boric acid—H_3BO_3). Careful examination of the daughter phases showed that some were unknown phases that were presumed to be other alkali borates, although visually similar to sassolite. These phases are typically colorless tabular grains (Figs. 1a and 1b) with a refractive index similar to sassolite ($n_\beta = 1.456$). The most striking phase showed a very strong Raman band at 547 cm^{-1}, quite unlike sassolite, which has characteristic Raman bands at 500 and 880 cm^{-1}. Moreover, some of these daughter phases are relatively large (up to 20 μm) platy crystals with apparently monoclinic morphology or ellipsoidal rounded grains (Fig. 1a). Heating experiments using a microscope heating stage demonstrates a high solubility of this daughter phase at relatively low temperatures. The Raman spectra for these new minerals do not correspond to any Raman spectra in the literature or the RRUFF database (Downs 2006). To identify these unknown phases, we undertook a systematic search of possible compounds, beginning with synthetic alkali borates, since most of the daughter phases are colorless and water-soluble, and B is a principal element in the inclusions as indicated by large sassolite crystals.

The material exists only as daughter minerals in melt and fluid inclusions, as crystals no larger than 20 × 11 μm. Moreover, because these new mineral phases are highly soluble in water and require high concentrations of the rare metals Cs and Rb, it is unlikely that they will ever be found outside melt or fluid inclusions. However, these phases do satisfy the criteria for valid mineral species (e.g., Nickel and Grice 1998), and the Commission of New Minerals, Nomenclature and Classification of the International Mineralogical Association (CNMNC IMA) has in place approval criteria to deal with minerals presenting particular difficulties, e.g., mineral phases in fluid inclusions.

Although controversial, these criteria have been met in the case of the two new minerals described for the first time, and the mineral phases described herein have been accepted by the

* E-mail: thomas@gfz-potsdam.de

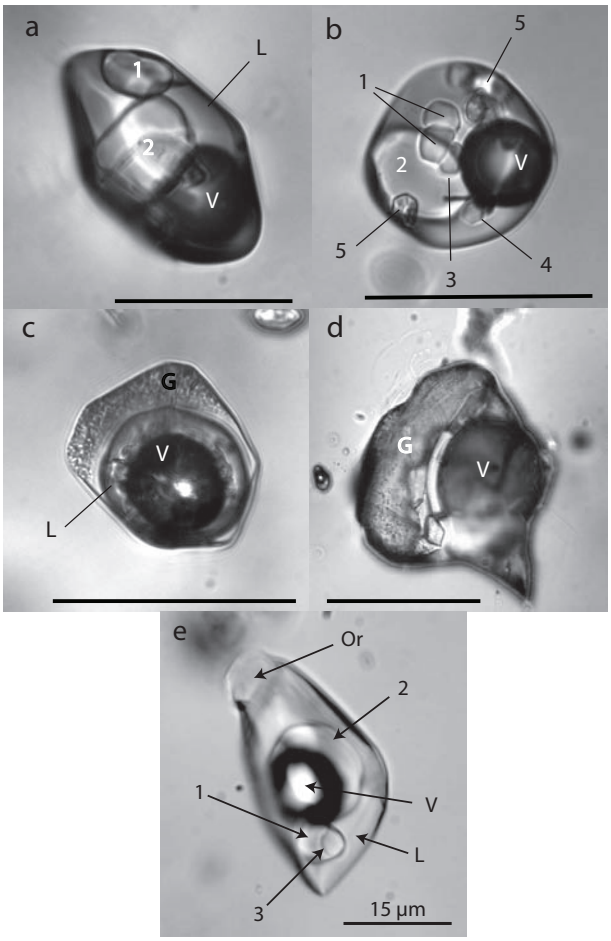

FIGURE 1. Type-B melt inclusions in graphic quartz from the Elba pegmatite, **a** and **b** are unheated, **c** and **d** are from the same growth zone, but re-homogenized at 700 °C, 2 kbar in 20 h using the cold-seal pressure vessel technique. 1 = ramanite-(Cs), 2 = sassolite, 3 = ramanite-(Rb), 4 = santite, 5 = topaz, V = vapor, L = boric acid saturated liquid, G = boron-rich silicate glass, scale bars are 50 µm. The melt inclusion in **c** is an unexposed equivalent of **d**, so the phase composition is preserved. The extremely high concentration of boric acid in the solution phase, as well as in bubble inside the glass, are characteristic—here formed by exsolution during quenching. The melt inclusion in **d** is composed of more or less stable boron- and cesium-rich glass, and a large bubble that is now exposed on the sample surface by polishing during preparation for the microprobe analysis. Significant amounts of boric acid were lost when this bubble was breached. Part **e** is representative of an unheated type-B melt inclusion in graphic quartz (similar to **a** and **b**), showing both new PBT minerals in a close contact, and demonstrating the relative relationship of their refractive indexes. Or = orthoclase, 1 = ramanite-(Cs), 2 = sassolite, 3 = ramanite-(Rb).

CNMNC as new mineral species. Ramanite-(Rb) (2007-006) and ramanite-(Cs) (2007-007) are Rb- and β-Cs-pentaborate tetrahydrates with the idealized chemical formula $RbB_5O_8 \cdot 4H_2O$ and $CsB_5O_8 \cdot 4H_2O$, respectively. Although the two phases are not isostructural, the same root names were accepted by the CNMNC because of their particular occurrence and their close association as daughter minerals in fluid and melt inclusions.

By the new criteria, the CNMNC is recognizing that Raman spectroscopy is a powerful tool for identifying phases, particularly those that are too small to apply conventional methods, e.g., daughter minerals in fluid and melt inclusions. We dedicate these new Rb- and Cs-phases to Sir Chandrasekhara Venkata Raman, since Raman spectroscopy was the key method in the identification of the minerals, and may be the basis of identifying many other new minerals. Chandrasekhara Venkata Raman was born on November 7, 1888 at Trichinopoly in Southern India and died on November 21, 1970. He obtained the Nobel Prize in Physics in 1930 for discovering the effect that bears his name.

The holotype material coming from a small pegmatite vein found near the village San Pietro in Campo on the Island of Elba, Italy is now deposited in the Museum of the Mining Academy Freiberg (Germany), catalog no. 81615 [ramanite-(Cs)] and 81616 [ramanite-(Rb)].

The aim of the present contribution is the identification of new Cs- and Rb-rich pentaborate minerals, as well as a short discussion of the extreme enrichment and fractionation of boron, cesium, and rubidium during pegmatite crystallization.

GEOLOGICAL CONSTRAINTS AND SAMPLE DESCRIPTION

The investigated sample from the collection of the Mining Academy of Freiberg is graphic granite from the small pegmatite vein called Il Prado (also known as Prato alla Valle) located 400 m south of the cemetery of the village San Piero in Campo on the Island of Elba, Italy. The sample was collected by G. Garbari from Trento in the last decade of the 19th century (detailed information about the origin of the studied sample is from Frederico Pezzotta, oral communication). This is also the type locality for rubicline (Teertstra et al. 1998). The Elba granite pegmatites form a pegmatite field along the eastern border of the Tertiary Mt. Capanne monzogranitic pluton (Pezzotta 2005) and belong to the so-called LCT (Li, Cs, and Ta) pegmatites (Černý 1991).

The sample consists of small smoky quartz crystals of hydrothermal origin, with overgrowths of cassiterite, as a final phase on the graphic granite (graphic intergrowths of K-feldspar and quartz). The graphic quartz contains two types of melt inclusions and a few secondary fluid inclusions. In addition to the melt inclusions and fluid inclusions in quartz, there are small euhedral (10–20 µm in diameter) solid inclusions of topaz, albite, orthoclase, pollucite, zircon, and xenotime-(Y). Unusually, we also found isolated sassolite, santite ($KB_5O_8 \cdot 4H_2O$) and other water-soluble alkali borate crystals trapped as mineral inclusions in the quartz matrix, demonstrating that the mineral-forming fluid was super-saturated with respect to boric acid. In feldspar, we could only determine sassolite as daughter mineral phase in highly concentrated fluid inclusions or type-B melt inclusions, because the broad Raman band of feldspar at about 512 cm^{-1} prevented the unequivocal determination of other constituents.

Unlike graphic quartz, the smoky quartz crystals contain only fluid inclusions with a vapor bubble, an aqueous solution, and sassolite daughter crystals. According to Thomas (2002) this inclusion type contains 18.5 mass% H_3BO_3 and 10.5 equivalent mass% NaCl. The homogenization temperature from 36 fluid inclusions is 292 ± 10 °C. The fluid inclusions in cassiterite homogenize at 386 °C with critical behavior. Some fluid inclusions in this cassiterite contain small arsenolamprite daughter crystals

(the orthorhombic form of native As), identified with Raman spectroscopy by the very strong bands at 219, 223.7, and 251.4 cm^{-1}. The above-mentioned mineral inclusions (topaz, albite, orthoclase, and pollucite) are absent in the hydrothermal quartz.

Type-A melt inclusions in quartz are small (up to 10 μm, mean 5 μm), completely crystallized, and contain a small vapor bubble. All unheated type-A melt inclusions show the characteristic Raman band at 880 cm^{-1}, indicating high concentrations of boric acid (Peretyazhko et al. 2004). For microprobe analyses of the inclusion glass the samples were re-homogenized at 600 and 700 °C and 2 kbar using the standard cold-seal pressure technique, with a 20 h run time (Figs. 1c and 1d).

In addition to the type-A melt inclusions there are extremely water-rich type-B melt inclusions, also very rich in boric acid. Inclusions of this type are significantly larger, commonly 40 to 50 μm in diameter. At room temperature they appear to be fluid inclusions with daughter crystals of sassolite, alkali borates, topaz, muscovite, anatase (TiO_2) and sometimes orthoclase and alkali pentaborates (e.g., Fig. 1a), and sometimes also grandidierite [(Mg, Fe^{2+})$Al_3(BO_3)(SiO_4)O_2$], identified by Raman spectroscopy (Downs 2006). Raman spectroscopic study of the unheated type-B melt inclusions shows that in addition to sassolite, daughter phases include tabular crystals of Cs pentaborate tetrahydrate, ramanite-(Cs), up to 20 μm in length and small crystals of Rb pentaborate tetrahydrate, ramanite-(Rb) and santite, up to 8 μm in diameter. Some crystals are corroded and rounded due to heating during preparation.

Because the sassolite-rich solutions in the studied inclusions generally have a refractive index $n_\beta \sim 1.456$ (often the thin sassolite crystals in the inclusions are almost completely invisible) the small crystals of santite and also sborgite ($NaB_5O_8 \cdot 5H_2O$) should show a negative relief, and ramanite-(Cs) and ramanite-(Rb) a positive relief. Ramanite-(Cs) crystals with overgrowths of ramanite-(Rb) demonstrate that the refractive index of ramanite-(Rb) is lower than that of ramanite-(Cs) and higher than 1.456 (Fig. 1e).

From well-formed inclusions and daughter phases, we have estimated the water, boron, cesium, rubidium, SiO_2, Al_2O_3, and F concentration in the type-B melt inclusions (third column in Table 1). SiO_2, however, is strongly underestimated, because the amount of SiO_2 crystallized out on the inclusion walls cannot be measured (Thomas et al. 2006b). We can only estimate the amount of SiO_2, which in a water-rich system disassociates on cooling into alkali borates and SiO_2.

Some type-B melt inclusions were re-homogenized by heating to establish bulk compositions. After re-homogenization they contain a relatively stable boron- and cesium-rich silicate glass, a fluid phase, and a bubble (e.g., Fig. 1d). Hydrothermal diamond anvil cell (HDAC) experiments have shown that this type of inclusion generally forms a homogeneous phase at high temperature that separates into these three phases with quenching/cooling (Thomas et al. 2006b, 2006d).

Table 1 gives the glass composition of the large type-B melt inclusion shown in Figure 1d. With Raman spectroscopy we observed that this glass is unstable under the electron beam. Before microprobe measurement we found a strong and broad Raman band at 880 cm^{-1}, characteristic of planar orthoborate three-coordinated boron mode $\nu_S(B^3\text{-O}$ in the melt [Thomas 2002]). The breakdown of this band during the microprobe measurement, demonstrates that in boron- and water-rich glasses the T-OH stretching or deformation vibration of hydrated boron species in glass are unstable (Fig. 2).

TABLE 1. Estimated composition of near-critical type-B melt inclusions (in mass%)

	Elba Island			Ehrenfriedersdorf/ Germany
	Type-B MI re-homogenized	Type-B MI† unheated	Estimated melt composition	Type-B MI re-homogenized
SiO_2	64.61	2.3	26.0#	61.00
TiO_2	d.l.		–	d.l.
B_2O_3	3.90	15.6‡	15.6	2.34
Al_2O_3	11.84	12.1§	12.1	16.00
FeO	0.03		0.3	d.l.
MnO	0.23		0.2	d.l.
MgO	0.01		–	d.l.
CaO	0.05		–	0.01
SrO	0.12		0.1	d.l.
Na_2O	1.41		3.7	5.69
K_2O	3.60		3.7	4.58
Rb_2O	0.46		0.5	2.90
Cs_2O	4.91	7.4	5.5‖	5.80
F	2.78	1.5	2.9	0.55
Cl	0.14		0.2	d.l.
P_2O_5	0.07		0.1	1.56
H_2O in glass	5.8*		–	n.a.
Bulk H_2O	33	46.0	30.0	(32)
Total	99.96		100.9	100.43
n	4	10		5

Notes: n = number of analyses; d.l. = below detection limit; n.a. = not analyzed. The inclusion in column 1 is the inclusion shown in Figure 1d.
* Water in the inclusion glass was determined with Raman spectroscopy (Thomas et al. 2006a), and the bulk water was estimated from volume measurements.
† The unheated type-B MI's mean: 14 boric acid, 8 cesium pentaborate, 2 topaz, 1 muscovite, and 1 K pentaborate (in vol%), maximum 35.2 mass% H_3BO_3 from the sassolite melting temperature of 120 °C according to the H_3BO_3-H_2O system (Linke 1958).
‡ A very conservative estimation from the sassolite and Cs pentaborate volume ratios.
§ Al_2O_3 = 5.1 mass% from topaz and muscovite, 7 mass% from the feldspars.
# At trapping conditions, the main amount of SiO_2 was fixed as $CsBSi_2O_6$ (see also Thomas et al. 2006c).
‖ According to London et al. (1998), this concentration gives an equilibrium temperature of 702 °C corresponding to the re-homogenization temperature.

It is a striking fact that re-homogenized type-B melt inclusions contain 5 mass% Cs_2O. The high Cs content partially stabilizes the glass structure permitting electron microprobe analyses of this relatively stable glass. Note however, that a significant amount of the water and boron in type-B melt inclusions could not enter into the glass structure (Figs. 1c and 1d) and remains as a residual aqueous bubble, which is lost if the inclusion is exposed.

Together with the high boron and fluorine concentration (about 4 and 3 mass%, respectively), it is clear that Cs preferentially partitions into the more water rich type-B melt. The boron concentration in the studied glass is strongly underestimated, since as noted significant boric acid is concentrated in the fluid phase of such inclusions, so there was a significant loss of boron as boric acid during sample preparation for the microprobe studies. The estimation of the true rubidium content is even more difficult, because the most Rb partitions preferentially into the liquid-water rich-phase (Rickers et al. 2006).

EXPERIMENTAL METHODS

Raman spectroscopy

Raman scattering was measured with the Jobin-Yvon LabRam HR800 spectrometer (grating: 2400 gr/mm), equipped with an Olympus optical microscope and a long-working-distance LMPlanFI 100×/0.80 objective, with the 488 nm excitation of a Coherent Ar^+ laser Model Innova 70C, a power of 200 mW (about 30 mW on sample), at a resolution ≤0.6 cm^{-1}. Each unpolarized spectrum results

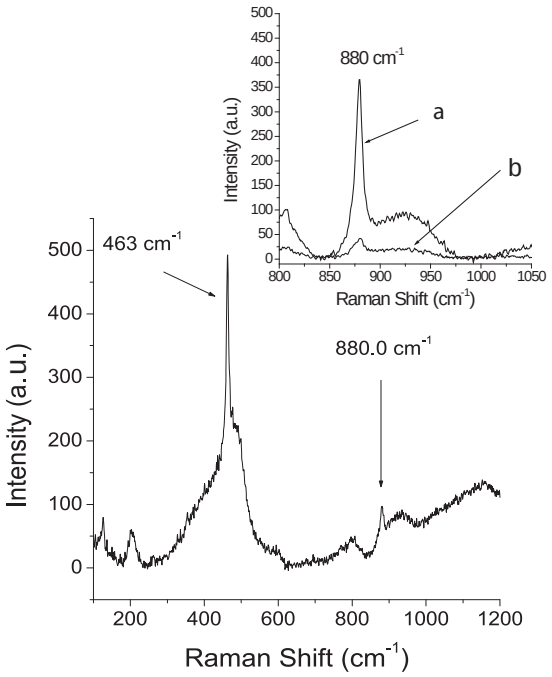

FIGURE 2. Raman spectrum in the frequency range 100 to 1200 cm^{-1} of the inclusion glass from the re-homogenized type-B melt inclusion; the inset is a close-up of the region between 800–1050 cm^{-1}. Spectrum a represents the glass prior to bombardment with the electron beam, and spectrum b shows the changed intensity after microprobe measurements. The sharp band at 463 cm^{-1} results from the quartz host. The broad band in the 850 to 1000 cm^{-1} region is characteristic for B- and water-rich silicate melts (Thomas 2002). The band at 880 cm^{-1} corresponds to planar orthoborate three-coordinated boron $\nu_s[B^3$-O mode (a)]. The integral intensity of this band is irreversibly reduced during the microprobe measurements as can be seen in the partial spectrum in the Raman shift region 800–1050 cm^{-1} (b).

from the accumulation of six acquisitions of 50 s each. The spectra were collected at a constant laboratory temperature (20 °C) with a Peltier cooled CCD detector and the position of the Raman bands were controlled and eventually corrected using the principal plasma lines in the Argon laser (Craig and Levin 1979; Berg and Nørbygaard 2006). The recommended and measured position of the plasma lines is given in Table 2. In the critical spectral region of the alkali pentaborate tetrahydrates between 50 and 1200 cm^{-1}, the shift is not larger than –0.6 cm^{-1}.

Reference samples

Because extraction of phases in the inclusions was not possible, we devised a plan to compare the Raman spectra of the unknown phases with those of synthetic standards of known chemical composition, symmetry, and cell parameters. There are good published Raman data for the Li, Na, and K borates (Janda and Heller 1980; Li et al. 1995). However, because practically no Raman spectra of hydrated Rb and Cs borates were found in the literature, we prepared synthetic Cs and Rb borates for comparison. The pentaborates tetrahydrates $M[B_5O_8 \cdot 4H_2O$ (M = Cs, Rb)] were obtained from aqueous solutions of dissolved M_2CO_3 and H_3BO_3 in stoichiometric proportions according to information given in Kocher (1966) and Tolédano (1964). With heating CO_2 was released and slow evaporation under weak heating led to the desired compounds in the form of white powders. The washed precipitate was dissolved in hot water (60 °C) and the β-Cs-pentaborate tetrahydrate was crystallized in small (50 µm) optically perfect plates by slow cooling All the reagents used in the synthesis were of analytic grade. The ideal formula of cesium pentaborate tetrahydrate (Cs-PBT) requires 36.41 mass% Cs_2O, 44.97 mass% B_2O_3, and 18.62 mass% H_2O and the corresponding rubidium pentaborate tetrahydrate (Rb-PBT) requires 27.52 mass% Rb_2O, 51.25 mass% B_2O_3, and 21.22 mass% H_2O.

The resulting very small crystals plates (up to 120 × 250 µm) of β-Cs and Rb pentaborates were checked with X-ray powder diffraction (see below). The Rb-PBT crystals showed a prismatic habit and most of them were twinned (Behm 1984a).

TABLE 2. Principal plasma lines in the 488 nm argon ion laser (according to Craig and Levin 1979), grating: 2400 gr/mm

Recommended shift (cm^{-1})	Measured shift (cm^{-1})	Δ (cm^{-1})
104.0	103.9	+0.1
221.5	221.9	–0.4
351.6	352.0	–0.4
380.3	380.5	–0.2
529.5	529.7	–0.2
560.6	560.9	–0.3
737.3	737.9	–0.6
1043.6	1044.1	–0.5
1056.9	1057.4	–0.5
3287.9	3288.2	–0.3
3509.4	3509.8	–0.4

Using the Becke Line method together with Cargille liquids (Cargille-Sacher Laboratories Inc., New York) the intermediate refractive index, n_β, were estimated for β-Cs-PBT and Rb-PBT (589 nm/20 °C) to be 1.520 and 1.498, respectively.

The Raman spectra of the main pentaborate tetrahydrate daughter phases beside sassolite are given in the Figures 3, 4, and 5. The Raman main frequencies of the alkali pentaborates hydrates are compiled according to Devarajan et al. (1976), Janda and Heller (1980), Li et al. (1995), and this work in Table 3. The observed main frequencies (in cm^{-1}) of Raman spectra of the synthetic Cs-PBT and Rb-PBT and natural ramanite-(Cs) and ramanite-(Rb) are compared in the Table 3. The assignment of the main Raman bands are from Devarajan et al. (1976), Janda and Heller (1980), Li et al. (1995), and this work.

The Rb and Cs hydrated tetraborates were also synthesized; however, these spectra are very different from the spectra of the described daughter minerals, and can be assumed not to exist in these inclusions because of the very high boric acid concentration (cf. Kocher 1966; Tolédano 1964). For example, the analytically important symmetric pulse vibrations of the tetraborate anion near 569 and 575 cm^{-1} for the hydrated tetraborates of Rb and Cs are absent in the new minerals.

The total water concentration in the glass of the type-B melt inclusions was determined by laser Raman microprobe by simple comparison with a known standard. For this, we used the broad and asymmetric H_2O-OH bands in the high-frequency region between 2800–4000 cm^{-1} according to Thomas et al. (2006a) and Thomas and Davidson (2006). Bulk water concentration is from estimations of the volume ratios and the Raman data (Table 1).

X-ray studies

For the XRD measurements, 1 mg of the sample material was ground in an agate mortar to grain sizes between 1 and 5 µm. Diluted with Elmer's White glue, the powder was mounted on a circular foil ("zero scattering"), which was subsequently covered with a second empty foil and placed into the transmission sample holder. To achieve a minimum of preferred orientation, the powder was stirred during drying.

The powder XRD patterns were collected using a STOE STADI P diffractometer ($CuK\alpha_1$ radiation) with a germanium (111) primary monochromator and a 7° position sensitive detector (PSD). Operating conditions of the normal-focus Cu X-ray tube were 40 kV, 40 mA, and a take-off angle of 6°. The spectra were recorded in transmission and in the 2θ range between 5–125° with a detector step interval of 0.1° resulting in a resolution of 0.01 °2θ. Counting times were adjusted to yield maximum intensities of 3000–5000 counts per second for each sample.

Rietveld refinements were performed using the GSAS software package (Larson and Von Dreele 2004) to determine unit cell and structural parameters, as well as phase proportions. The peaks were defined as pseudo-Voigt with a variable Lorentzian character. The peak full-width at half maximum height (FWHM) was varied as a function of 2θ using the parameters "GU," "GV," and "GW" (Caglioti et al. 1958). For the Lorentzian character the parameters "LX" and "LY" were applied. The recorded peaks were highly symmetric due to the geometry of the STADI P diffractometer, therefore, no parameters describing the asymmetry of the peaks had to be used. The background was fitted by 4 parameters for function TYPE 1 (Chebyschev polynomial). The diffuse background due to the amorphous foil and glue for the preparation was modeled with the diffusive scattering function (TYPE 1 within diffusive scattering option). The preferred orientation was corrected with the use of spherical harmonic functions (Bunge 1982; Von Dreele 1997). The Durbin-Watson statistic is within the range of 1.1 (Cs-PBT) to 1.9 (Rb-PBT). χ^2 values range from 1.1 to 1.4. R_{wp} and R_p are 0.062 and 0.048 for Cs-PBT and 0.084

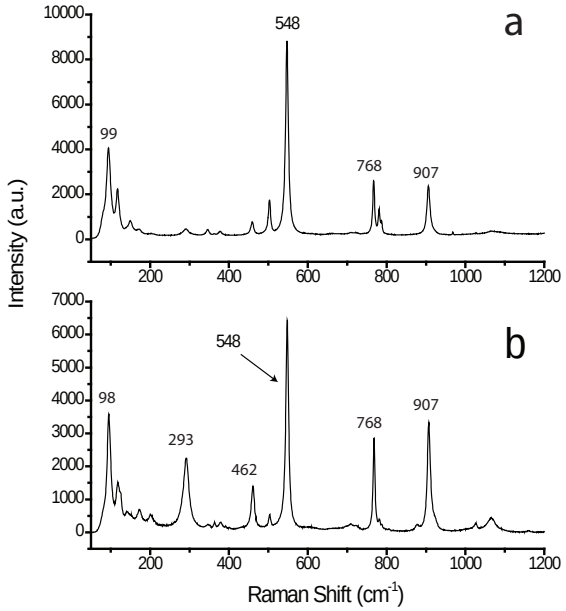

FIGURE 3. Comparison of Raman spectra of synthetic and natural Cs pentaborate tetrahydrate. (**a**) Synthetic Cs pentaborate tetrahydrate. (**b**) Natural ramanite-(Cs) in an inclusion in graphic quartz from the Elba pegmatite. Note that the higher peak at 462.3 cm^{-1} is influenced by the strong Raman band of the quartz matrix, and the bands at 292 and 768 cm^{-1} show extensive intensity changes depending upon the sample orientation. For the apparent differences between the natural and synthetic material see Table 3. Peak labels (in cm^{-1}) refer to the diagnostic bands.

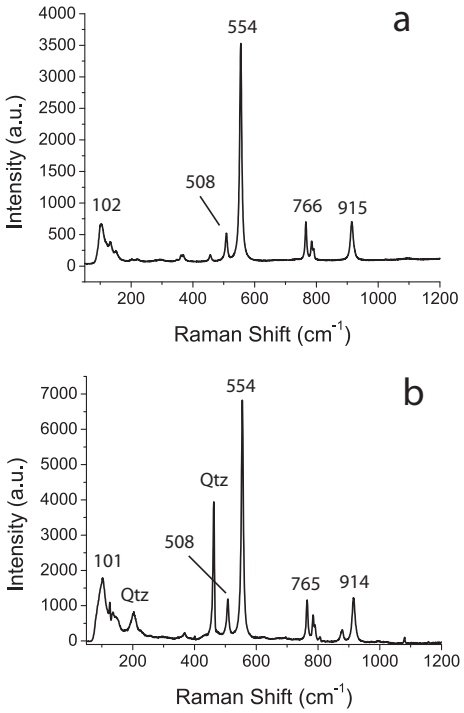

FIGURE 4. Comparison of Raman spectra of synthetic and natural Rb pentaborate tetrahydrate. (**a**) Synthetic Rb pentaborate tetrahydrate and (**b**) natural ramanite-(Rb) in an inclusion in graphic quartz from the Elba pegmatite. Peak labels (in cm^{-1}) refer to the diagnostic bands. Qtz = strong Raman bands of the quartz matrix.

and 0.063 for Rb-PBT (see Tables 4 and 5).

The crystallographic and structural data of the α- and β-cesium pentaborate tetrahydrates as well as Rb-pentaborate tetrahydrate are given in Behm (1984a, 1984b) and Penin et al. (2002) and a survey of alkaline and pseudo-alkaline borates is presented by Touboul et al. (2003).

Electron microprobe

Homogeneous glasses in type-B melt inclusions were analyzed by the JEOL JXA-8500F electron microprobe, using chips mounted on glass disks and polished under oil. Analyses were performed in the wavelength-dispersive mode under the following conditions: 15 kV acceleration voltage, 20 nA (for boron 40 nA) beam current, spot size of 5–40 μm. Details are given in Thomas et al. (2003, 2006d). Boron was analyzed at 10 kV and 40 nA in the trace element mode. LaB_6 was used as internal standard.

Prior to a detailed Raman study of the daughter phases in the unheated type-B melt inclusions and fluid inclusions we determined the composition of a type-B melt inclusions in the same growth zone (Table 1), where the inclusions with the unknown daughter phases appear (for this we used a parallel sample chip). Table 1 gives the composition of the type-B melt inclusion glass from the Ehrenfriedersdorf pegmatite for comparison (see "Reference samples"). This composition was the starting point for the synthesis of hydrated alkali borates.

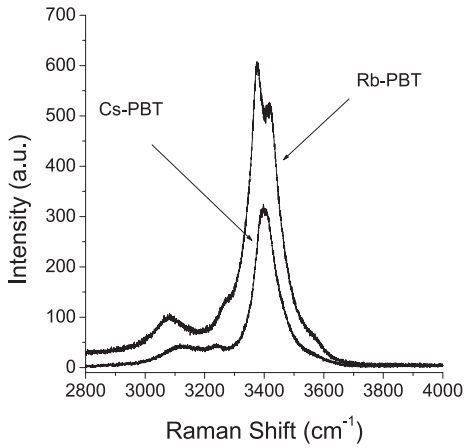

FIGURE 5. Raman spectra of Cs and Rb pentaborate tetrahydrate (Cs-PBT and Rb-PBT) in the high-frequency range.

NEW CS AND RB MINERALS

The Raman spectra of the newly discovered daughter crystals (Fig. 1) corresponds very well (Figs. 3 and 4; Table 3) with the synthetically produced β-cesium pentaborate tetrahydrate (β-$CsB_5O_8 \cdot 4H_2O$) (Penin et al. 2002; Touboul et al. 2003) and Rb-pentaborate tetrahydrate (Behm 1984a). The most intense features of both the natural and synthetic phases are the symmetric pulse vibration of the Cs pentaborate anion at 547 cm^{-1} and the bands at 95, 768, and 907 cm^{-1}. These bands are the characteristic Raman signature of β-Cs pentaborate (Fig. 3). Since each band in a Raman spectrum represents the interaction of the incident light with the sample and because the vibrations of the sample are controlled by the sizes, valences, and masses of the atomic species, the bond forces between the atoms, and the symmetry of their arrangement in the crystal structure the Raman spectra are highly specific for the sample and can be used for the identification and structural characterization of unknown samples. Therefore, the similarities of the Raman spectra between natural ramanite-(Cs) and ramanite-(Rb), and synthetic β-Cs

TABLE 3. Raman main frequencies (in cm^{-1}) of the synthetic and natural alkali pentaborates hydrates

Synthetic pentaborate hydrates							Natural pentaborate tetrahydrates in inclusions			Assignment
Li	Na	K	Rb	α-Cs	β-Cs		Rb	β-Cs		
		95	97							
	121‡	**107**	**102**		**98**	**99**	**101**	**94**	**98**	ring torsion
		(133)	(132)	(119)	(118)	(120)		118	(119)	ring torsion
		(297)	(295)		(292)	**292**		292	**293**	δ OBO tetrahedral bend
		(371)	(368)		(347)					ν B-O + δ OBO
464	464	456	456		(460)	460		462*		δ OBO + γ BO_3
492	493	509	508	(503)	504	(504)	508	503	(501)	δ OBO ring
530	**529**	**556**	**554**	**549**	**548**	**549**	**554**	**548**	**548**	ν_P-$[B_5O_6(OH)_4]^-$†
779	773	**765**	**766**	767	768	**768**	765	768	768	ν_S ($B_{(4)}$-O)
796		786	784	(782)	783	(781)	785	781	(780)	ν B-O + δ BOB ring
	856									ν_S ($B_{(4)}$-O)
924	922	**918**	**915**	**907**	**907**	**907**	**914**	**906**	**907**	ν_S ($B_{(3)}$-O)
		(1250)	(1240)		(1221)					δ(O-H)
		(1365)	(1366)	**1339**	(1360)				(1484)	ν_a external stretch B-O
				1603						ν_a external stretch B-O
		(3058)	(3084)	(3108)	(3117)	**3116**			**3119**	ν(O-H)
			(3274)	(3230)	(3225)					ν(O-H)
		3364	**3373**				**3374**			ν(O-H)
	3459‡	**3436**	**3425**	**3406**	**3404**	**3396**	**3426**	**3394**	**3396**	ν(O-H)
			(3587)			(3568)				ν(O-H)

Notes: Data from Devarjan et al. (1976), Janda and Heller (1980), Li et al. (1995), and this work, as well as the observed main frequencies of the natural Rb- and Cs-pentaborate tetrahydrates (PBT) as daughter mineral phases in fluid and melt inclusions. The bold numbers are the strongest Raman bands and the numbers in the brackets are very weak. The bands at 292 and 768 cm^{-1} of the β-Cs-PBT show extensive intensity changes depending upon the sample orientation.
* The band at 462.3 cm^{-1} is influenced by the strong Raman band of the quartz matrix.
† The bands between 529 and 556 cm^{-1} are very strong and represent symmetric pulse vibration of the pentaborate anion and can be used for the discrimination between pentaborate and tetraborate compounds.
‡ Complemented by this work.

and Rb-PBT can be used for simple, rapid phase analysis, in a similar way as performed by X-ray powder diffraction (Burke 2001; Lutz and Haeusler 1999; Nasdala et al. 2004).

The identity of the synthetic standards was confirmed by powder X-ray diffraction (Figs. 6 and 7; Tables 4 and 5). In Tables 4 and 5, the results of X-ray measurements are compared with the calculated data using the Rietveld-Software "PowderCell 2.3" (Kraus and Nolze 1999). From this comparison an excellent agreement between the synthetically produced β-Cs- and Rb-PBT and the structure data given by Penin et al. (2002) for Cs-PBT and Behm (1984a) for Rb-PBT are apparent.

For the monoclinic β-Cs-PBT, the following cell parameters were obtained (Table 6): a = 8.130(2) Å, b = 12.045(3) Å, c = 11.792(3) Å, β = 93.34°; and V = 1152.85(60) $Å^3$; space group $C2/c$. The calculated density is 2.230 g/cm^3. Using the program PowderCell 2.3 we can estimate that only traces of the α-phase can be present in the β-phase of the Cs-PBT.

The monoclinic α-Cs-PBT was obtained in a different way by Behm (1984b), who used ionic exchange from an aqueous sodium pentaborate solution to which cesium chloride had been added. This demonstrates that Cs-PBT is more stable than Na-PBT (since simple ion exchange reaction is only possible if one compound is more stable as the other), and that the phase produced by this different method is not identical with the β-Cs-PBT, which can also be seen from the main bands in the Raman spectra (Table 3).

For the orthorhombic Rb-PBT, the following cell parameters were obtained (Table 6): a = 11.304(1) Å, b = 10.963(1) Å, c = 9.337(1) Å, and V = 1157.14(11) $Å^3$; space group $Aba2$. The calculated density is 1.949 g/cm^3 (Behm 1984a).

According to Touboul et al. (2003), the synthetically produced Cs and Rb borates correspond to the monoclinic β-$CsB_5O_8 \cdot 4H_2O$ and the orthorhombic $RbB_5O_8 \cdot 4H_2O$, respectively.

β-$CsB_5O_8 \cdot 4H_2O$ crystallizes in the monoclinic system with the $C2/c$ space group and is not isostructural with any other alkaline or pseudo-alkaline pentaborates. Therefore this phase should be the end-member phase. The agreement with the synthetic material is so good that discrimination is clearly possible, thus the naturally occurring β-$CsB_5O_8 \cdot 4H_2O$ phase appears nearly free of K and Rb.

According to Penin et al. (2002), $Li[(B_5O_6)_4(OH)_4] \cdot 3H_2O$ and

TABLE 4. X-ray powder-diffraction data of ramanite-(Cs)

Measured			Calculated (PowderCell 2.3)*		
hkl	*d* (Å)	*I* (rel.)	*hkl*	*d* (Å)	*I* (rel.)
020	6.023	100	020	6.022	94
$11\bar{1}$	5.969	19	$\bar{1}11$	5.969	21
002	5.886	29	002	5.886	23
111	5.725	20	111	5.725	23
021	5.362	26	021	5.362	28
022	4.210	31	022	4.209	27
200	4.058	23	200	4.058	21
130	3.599	15	130	3.599	15
$13\bar{1}$	3.467	26	$\bar{1}31$	3.467	25
$11\bar{3}$	3.464	24	$\bar{1}13$	3.464	29
$20\bar{2}$	3.436	10	$20\bar{2}$	3.436	14
220	3.366	83	220	3.366	100
113	3.321	33	113	3.321	36
$22\bar{1}$	3.278	53	$22\bar{1}$	3.278	56
132	3.036	15	132	3.036	22
004	2.943	49	004	2.943	39
041	2.917	16	041	2.917	24
$31\bar{1}$	2.608	12	$\bar{3}11$	2.607	21
043	2.389	12	043	2.389	16
$22\bar{4}$	2.270	12	$\bar{2}24$	2.270	19
224	2.164	12	224	2.164	16
152	2.138	12	152	2.138	14

Note: Measurement time was 18 s per 0.1° step and the wavelength 1.5404785 Å.
* The calculation was performed with the data from this work given in Table 6. DW = 1.1, χ^2 = 1.4, R_{wp} = 0.062, R_p = 0.048 $R_p = \sum |y_i^{obs} - y_i^{calc}| / \sum y_i^{obs}$,

$R_{wp} = \sqrt{\sum w_i \left(y_i^{obs} - y_i^{calc}\right)^2 / \sum w_i \left(y_i^{obs}\right)^2}$,

$\chi^2 = \sum w_i \left(y_i^{obs} - y_i^{calc}\right)^2 / (N - P)$, y intensity, w = 1/y weighting factor, N – P = observations (step intervals) – least-squares parameters, DW = Durbin-Watson statistics.

TABLE 5. X-ray powder-diffraction data of ramanite-(Rb)

Measured			Calculated (PowderCell 2.3)*		
hkl	*d* (Å)	*I* (rel.)	*hkl*	*d* (Å)	*I* (rel.)
111	6.018	34	111	6.017	32
020	5.481	84	020	5.482	93
002	4.669	18	002	4.668	15
220	3.935	18	220	3.935	18
202	3.600	10	202	3.599	9
022	3.554	100	022	3.554	100
122	3.391	64	122	3.390	63
311	3.329	37	311	3.329	35
131	3.259	27	131	3.258	29
222	3.009	24	222	3.009	24
113	2.894	29	113	2.894	29
400	2.826	45	400	2.826	38
331	2.525	23	331	2.525	27
042	2.364	13	042	2.364	16
313	2.344	19	313	2.344	19
004	2.334	12	004	2.334	11
133	2.319	10	133	2.219	12
422	2.212	31	422	2.212	31
242	2.181	14	242	2.180	18
204	2.158	13	204	2.157	12
511	2.154	19	511	2.154	17
151	2.097	15	151	2.097	19
224	2.008	13	224	2.008	12

Note: Measurement time was 5 s per 0.1° step and the wavelength 1.5406493 Å.
* The calculation was performed with the data from this work given in Table 6. DW = 1.9, $\chi^2 = 1.1$, $R_{wp} = 0.084$, $R_p = 0.063$ $R_p = \sum|y_i^{obs} - y_i^{calc}| / \sum y_i^{obs}$,

$R_{wp} = \sqrt{\sum w_i \left(y_i^{obs} - y_i^{calc}\right)^2 / \sum w_i \left(y_i^{obs}\right)^2}$,

$\chi^2 = \sum w_i \left(y_i^{obs} - y_i^{calc}\right)^2 / (N - P)$, y intensity, w = 1/y weighting factor, N – P = observations (step intervals) – least-squares parameters, DW = Durbin-Watson statistics.

$Na[(B_5O_6)_4(OH)_4]\cdot 3H_2O$ are isostructural and crystallize in the monoclinic system with the *C*2/*c* space group. $KB_5O_8\cdot 4H_2O$ and $RbB_5O_8\cdot 4H_2O$ are isostructural and crystallize in the orthorhombic system with the *Aba*2 space group. Therefore it is possible that K may replace Rb in ramanite-(Rb). This is generally the case in fluid inclusions; however, in type-B melt inclusions we found both end-members [ramanite-(Rb) and santite]. This identification is possible because the Raman band positions differ significantly from each other. Although the low-frequency range (100–1200 cm^{-1}) peaks for santite and ramanite-(Rb) are close to the 50% criterion of Nickel and Grice (1998) and are valid only for extreme end-member compositions (918–914 cm^{-1}), in the high-frequency range (3390–3460 cm^{-1}) peaks are sufficiently separated for complete confidence, even on less modern instruments. The presence of both phases is possible because the crystallization sequence of daughter minerals in melt inclusions differs from the sequence in fluid inclusions.

Table 6 gives the crystallographic data for the cesium and rubidium pentaborate tetrahydrate together with the data of the very rare minerals santite and sborgite from the compilation in Touboul et al. (2003) and the data obtained for the daughter crystals in the Elba inclusions.

We stress here that we are comparing synthetic standards against naturally occurring minerals, found in complex multicomponent fluids, inside inclusions in a host mineral. Inevitably this introduces complexity, for example Raman peaks influenced by the host mineral (Figs. 3 and 4). However, the match is sufficient to show that the new minerals are indeed β-cesium pentaborate tetrahydrate, and rubidium pentaborate tetrahydrate. The X-ray data are simply intended to show that the synthetic standards actually correspond to the already well-characterized phases.

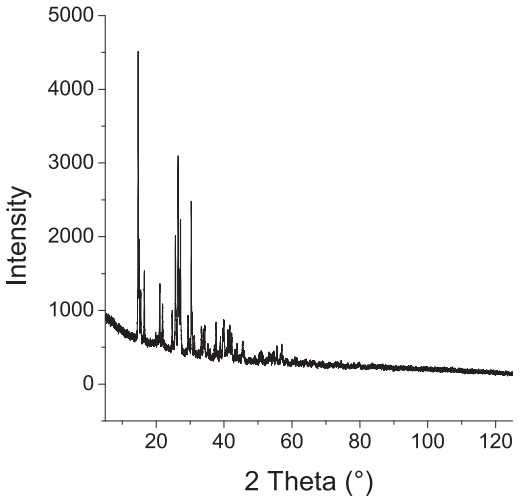

FIGURE 6. X-ray powder diffraction patterns of the synthetic Cs pentaborate tetrahydrate.

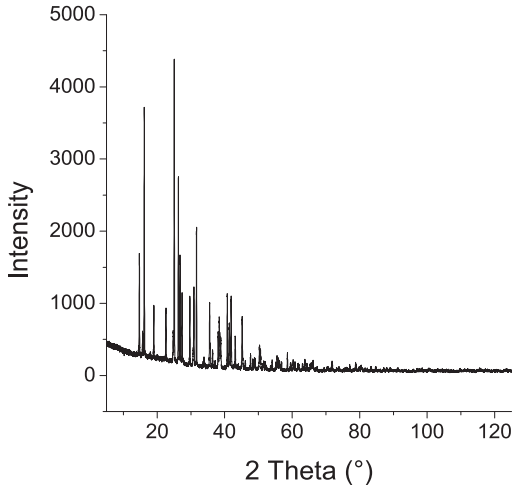

FIGURE 7. X-ray powder diffraction patterns of the synthetic Rb pentaborate tetrahydrate.

RAMANITE-(CS) AND RAMANITE-(RB)

Although optically indistinguishable, ramanite-(Cs) and ramanite-(Rb) have distinctive Raman spectra allowing simple and definitive identification from the clutter of almost indistinguishable translucent phases found in many hypersaline fluid inclusions. We have identified ramanite-(Cs) and ramanite-(Rb) in melt inclusions in pegmatite quartz from the Elba Island, Italy, as well as ramanite-(Cs) in the Ehrenfriedersdorf pegmatite, in topaz of the Wolfsgrün pegmatite from the Eibenstock granite in the W-Erzgebirge, Germany, in the smoky quartz from the Malkhan pegmatite, Transbaikalia (Russia), in hambergite from the Mika pegmatite, Rangkul pegmatite field, eastern Pamirs, Tajikistan and a solid-solution series of $(Rb,K)B_5O_8\cdot 4H_2O$ in topaz from Gross Spitzkoppe, Namibia. An important criterion for the identification of alkali pentaborate hydrates in fluid and melt inclusions is the existence of large sassolite daughter crys-

TABLE 6. Unit-cell parameters and symmetry of some alkali pentaborates

Structural formula	*a* (in Å)	*b* (in Å)	*c* (in Å)	β (in deg)	*V* (in Å^3)	Space group	Natural analog
α-$Cs[B_5O_6(OH)_4]\cdot 2\ H_2O$*	11.584	7.174	13.959	94.61	1156.3	$P2_1/c$	
β-$Cs[B_5O_6(OH)_4]\cdot 2\ H_2O$*	8.160	12.140	11.860	93.00	1173.3	*C*2/*c*	ramanite-(Cs)
β-$Cs[B_5O_6(OH)_4]\cdot 2\ H_2O$†	8.130(2)	12.045(3)	11.792(3)	93.34(2)	1152.85(60)	*C*2/*c*	ramanite-(Cs)
$Rb[B_5O_6(OH)_4]\cdot 2\ H_2O$*	11.302	10.962	9.335		1156.6	*Aba*2	ramanite-(Rb)
$Rb[B_5O_6(OH)_4]\cdot 2\ H_2O$†	11.304(1)	10.963(1)	9.337(1)		157.14(11)	*Aba*2	ramanite-(Rb)
$K[B_5O_6(OH)_4]\cdot 2\ H_2O$*	11.062	11.175	9.041		1117.6	*Aba*2	santite
$Na[B_5O_6(OH)_4]\cdot 3\ H_2O$*	11.097	16.435	13.786	115.02	2278.4	*C*2/*c*	sborgite
$Li[B_5O_6(OH)_4]\cdot 3\ H_2O$*	10.884	16.001	13.286	112.71	2134.5	*C*2/*c*	

* Touboul et al. (2003).
† This work.

tals, demonstrating high concentrations of boric acid.

Thus far we have used Raman spectroscopy to identify Na, K, Rb, and Cs pentaborates. However, in samples from Elba and the Malkhan pegmatite, Transbaikalia we have evidence of the existence of Li pentaborates, although we have not performed systematic studies, and the identification remains tentative.

DISCUSSION

Formation of the ramanite-(Cs) and ramanite-(Rb)-bearing inclusions

During the crystal growth of graphic pegmatite quartz, small droplets of water, boric acid, and rare alkali-rich pegmatite-forming melt were trapped. Upon cooling from about 700 °C down to room temperature, such water-rich melts are not stable and break down into their component parts, which are more stable at lower temperatures. Thus, these apparent "fluid inclusions" are actually melt inclusions (Thomas et al. 2006d), and since the crystallization processes are slow, they are a type of fractional crystallization. The first phases that are formed are molecular water and boric acid, then the mineral-phases orthoclase and topaz, and later ramanite-(Cs), followed by ramanite-(Rb) and others. During this crystallization process, quartz is deposited on the inclusion wall (becoming indistinguishable against the host quartz phenocryst) and forcing the existing fluids and crystal phases into the center of the inclusion, producing the appearance of a fluid inclusion.

Ramanite-(Rb) and santite, solid solutions, and end-members

Two different inclusion types exist in hambergite from the Mika pegmatite: primary inclusions formed from type-B melt inclusions (e.g., Fig. 1b) and secondary fluid inclusions. In the primary inclusions, we have detected ramanite-(Cs) and ramanite-(Rb) end-members (Tables 3 and 6), and, in the secondary fluid inclusions, we found solid solutions between the K- and Rb-phases [(Rb,K) $B_5O_8\cdot 4H_2O$]. This apparent inconsistency is a result of significant differences between the crystallization of daughter crystals in a fluid inclusion, and in a water-rich melt inclusion. In a fluid inclusion, all elements are present from the beginning in the same environment—the solution. Temperature, concentration, and the stability of the complexes determine the type of daughter phases. In complete contrast, the coexistence of santite and ramanite-(Rb) daughter crystals in the same melt inclusions is a function of the crystallization sequence in type-B melt inclusions. In a water-rich type-B melt inclusion, the first effect is a large amount of Si crystallizing as quartz, which is deposited at the inclusion wall, forming an apparent fluid inclusion. The next step is crystallizing stable silicates such as muscovite and feldspars as daughter minerals, which consume most of the K and Al. One of the last silicate minerals to crystallize is topaz, consuming most of the F and the last Al and Si. During the crystallization of the silicates, the amount of water increases together with B and the rare alkalis. Due to the very high concentration of boric acid Rb and Cs remain preferentially in the solution. The Rb concentration in the coexisting feldspars is relatively low. During further cooling, the ramanite-(Cs) and ramanite-(Rb) crystallize directly from the solution in the order: first ramanite-(Cs), then ramanite-(Rb). Crystallization of the relatively stable ramanite-(Cs) and ramanite-(Rb) also increases the K and Na concentration, forming santite and NaCl, because the solubility of K-PBT is significantly higher than the solubility of ramanite-(Rb).

If we dissolve the separate alkali pentaborates by heating on a microscope heating stage, only the ramanite-(Cs) crystallizes on cooling as a pure end-member phase. After that, ramanite-(Rb) forms a solid solution between santite and ramanite-(Rb). This can also be shown experimentally; for example adding potassium hydroxide to a ramanite-(Rb) solution always yields a solid solution during cooling. At high K concentration, we can then detect the formation of hydrated K-tetraborate, recognizable by the very strong Raman-band at 570 cm^{-1}.

Cs and Rb in pegmatite-forming magmas

Apart from the data from the Malkhan pegmatite field/Transbaikalia (Peretyazhko et al. 2004), the concentrations of boron and cesium presented here are currently the highest described in inclusions of natural pegmatite-forming melts or fluids. It should also be noted that the measured concentrations of Rb are also high. The most feasible explanation for such high concentrations is fractional crystallization, and subsequent liquid-liquid immiscibility, as indicated by the co-genetic relatively low Cs and Rb type-A and the Cs- and Rb-rich type-B melt inclusions.

Since we have observed isolated pollucite and sassolite crystals as mineral inclusions in the quartz from the inner part of the graphic pegmatite, we can infer that the pegmatite-forming melt or silicate-rich fluid was pollucite- and sassolite-saturated, which is also supported by the glass composition. According to London et al. (1998), an equilibrium temperature of about 670 °C is consistent with the 4.91 mass% Cs_2O in the inclusion glass (Table 1; column 1), which corresponds to our rough estimation of the inclusion trapping temperature. The value of 7.4 mass% Cs_2O by volume (Table 1; column 3) is possibly an overestimate, since it would give an equilibrium temperature of 815 °C. Note however, that addition of SiO_2 now crystallized on the inclusion

wall would dilute the Cs concentration.

As noted, the type-B melt inclusion glass is unstable, and breaks down into its simple component parts (boric acid and alkali borates) in the presence of high water and boron concentrations. Fluorine, primarily present as fluoroboric acid and its hydroxyl derivatives, on cooling forms topaz with available Si and Al (Thomas et al. 2005). Any remaining silica is deposited epitaxially on the inclusion walls. As a result of this transformation the former melt inclusions now resemble fluid inclusions (Fig. 1a before, and Fig. 1c after homogenization).

At high boric acid and relatively low alkali concentrations the propensity toward the formation of pentaborates is very strong (cf. Gmelins 1926). Therefore the formation of cesium pentaborate tetrahydrate ($CsB_5O_8 \cdot 4\ H_2O$) at high boric acid and relatively high concentrations of cesium (as demonstrated by microprobe) is not surprising.

ACKNOWLEDGMENTS

We thank the staff of the Museum of the Mining Academy of Freiberg, Germany, for the provision of the sample from the Island of Elba and Gerhard Berger (GFZ Potsdam) for many doubly polished sections of this sample. We also thank Federico Pezzotta for his detailed information about the origin of the studied sample. We are grateful to Dieter Rhede and Oona Appelt (GFZ Potsdam) for assistance with the EMP measurements. Thanks go also to Matthias Gottschalk (GFZ Potsdam) for assistance during the X-ray studies. Special thanks go to Ernst Burke for his strong support and encouragement during the CNMMN approval process. The manuscript was improved thoroughly by the suggestions and comments of an anonymous reviewer and George Harlow as well as by the associate editor Edward Grew.

REFERENCES CITED

Behm, H. (1984a) Rubidium pentaborate tetrahydrate $Rb[B_5O_6(OH)_4]\cdot 2H_2O$. Acta Crystallographica, C40, 217–220.

——— (1984b) Structure determination on a twinned crystal of cesium pentaborate tetrahydrate $Cs[B_5O_6(OH)_4]\cdot 2H_2O$. Acta Crystallographica, C40, 1114–1116.

Berg, R.W. and Nørbygaard, T. (2006) Wavenumber calibration of CCD detector Raman spectrometers controlled by sinus arm drive. Applied Spectroscopy Reviews, 41, 165–183.

Bunge, H.-J. (1982) Texture Analysis in Materials Science: Mathematical Methods. Butterworths, London.

Burke, E.A.J. (2001) Raman microspectrometry of fluid inclusions. Lithos, 55, 139–158.

Caglioti, G., Paoletti, A., and Ricci, F.P. (1958) Choice of collimators for crystal spectrometer for neutron diffraction. Nuclear Instruments, 3, 223–228.

Černý, P. (1991) Rare element granitic pegmatites. Part 1: Anatomy and internal evolution of pegmatite deposits. Geoscience Canada, 18, 49–67.

Craig, N.C. and Levin, I.W. (1979) Calibrating Raman spectrometers with plasma lines from the argon ion laser. Applied Spectroscopy, 33, 475–476.

Devarajan, V., Gräfe, E., and Funck, E. (1976) Raman spectrum and normal coordinate analysis of pentaborate ion (B_5O_{10}) in potassium pentaborate tetrahydrate. Spectrochimica Acta, 32A, 1225–1233.

Downs, R.T. (2006) The RRUFF Project: an integrated study of the chemistry, crystallography, Raman and infrared spectroscopy of minerals. Program and Abstracts of the 19th General Meeting of the International Mineralogical Association in Kobe, Japan. O03-13.

Gmelins Handbuch der anorganischen Chemie (1926) System-Nummer 13: Bor. Verlag Chemie Leipzig-Berlin (8. Auflage), 142 p.

Janda, R. and Heller, G. (1980) IR- and Ramanspektren isotop markierter Tetra-und Pentaborate. Spectrochimica Acta, 36A, 997–1001.

Kocher, J. (1966) Étude des borates de rubidium et de césium. Revue de Chimie minérale, 3, 209–257.

Kraus, W. and Nolze, G. (1999) PowderCell for Windows: Structure visualisation/manipulation, powder pattern calculation and profile fitting. Bundesanstalt für Materialforschung und-prüfung (BAM), version 2.3.

Larson, A.C. and Von Dreele, R.B. (2004) Generalized structure analysis system (GSAS). Alamos National Laboratory Report LAUR 96–748. Los Alamos National Laboratory, New Mexico.

Li, J., Xia, S., and Gao, S. (1995) FT-IR and Raman spectroscopic study of hydrated borates. Spectrochimica Acta, 51A, 519–532.

Linke, W.F. (1958) Solubility of boric acid in water. In Solubilities—Inorganic and Metal-Organic compounds. A compilation of Solubility Data from the Periodical Literature, vol. I, p. 261–262. D. van Nostrand Company, Inc., Princeton, New Jersey.

London, D., Morgan VI, G.B., and Icenhower, J. (1998) Stability and solubility of pollucite in the granite system at 200 MPa H_2O. The Canadian Mineralogist, 36, 497–510.

Lutz, H.D. and Haeusler, H. (1999) Infrared and Raman spectroscopy in inorganic solids research. Journal of Molecular Structure, 511–512, 69–75.

Nasdala, L., Smith, D.C., Kaindl, R., and Ziemann, M.A. (2004) Raman spectroscopy: Analytical perspectives in mineralogical research. In A. Beran and E. Libowitzky, Eds., Spectroscopic Methods in Mineralogy, 6, p. 281–343 (Chapter 7). European Mineralogical Union Notes in Mineralogy, Eötvös University Press, Budapest.

Nickel, E.H. and Grice, J.D. (1998) The IMA commission on new minerals and mineral names: Procedures and guidelines on mineral nomenclature. The Canadian Mineralogist, 36, 1–14.

Penin, N., Seguin, L., Gérand, B., Touboul, M., and Nowogrocki, G. (2002) Crystal structure of a new form of $Cs[(B_5O_6)_4(OH)_4]\cdot 2H_2O$ and thermal behavior of $M[B_5O_6(OH)_4]\cdot 2H_2O$ (M = Cs, Rb, Tl). Journal of Alloys and Compounds, 334, 97–109.

Peretyazhko, I.S., Zagorsky, V.Y., Smirnow, S.Z., and Mikhailov, M.Y. (2004) Conditions of pocket formation in the Oktyabrskaya tourmaline-rich gem pegmatite (the Malkhan field, Central Transbaikalia, Russia). Chemical Geology, 210, 91–111.

Pezzotta, F. (2005) Contribution to the study of the petrogenesis of granitic pegmatites; the example of the LCT pegmatites of Elba Island (Tyrrhenian Sea, Italy). In Crystallization Processes in Granitic Pegmatites, International Meeting in Cavoli, Elba Island, Italy, May 23–28, 2005, 3 p.

Rickers, K., Thomas, R., and Heinrich, W. (2006) The behavior of trace elements during the chemical evolution of the H_2O-, B-, and F-rich granite-pegmatite-hydrothermal system at Ehrenfriedersdorf, Germany: a SXRF study of melt and fluid inclusions. Mineralium Deposita, 41, 229–245.

Teertstra, D.K., Černý, P., Hawthorne, F.C., Pier, J., Wang, L., and Ewing, R.C. (1998) Rubicline, a new feldspar from San Piero in Campo, Elba, Italy. American Mineralogist, 83, 1335–1339.

Thomas, R. (2002) Determination of the H_3BO_3 concentration in fluid and melt inclusions in granite pegmatites by laser Raman microprobe spectroscopy. American Mineralogist, 87, 56–68.

Thomas, R. and Davidson, P. (2006) Progress in the determination of water in glasses and melt inclusions with Raman spectroscopy: A short review. Zeitschrift für geologische Wissenschaften, Berlin 34, 159–163.

Thomas, R., Förster, H.-J., and Heinrich, W. (2003) The behavior of boron in a peraluminous granite-pegmatite system and associated hydrothermal solutions: a melt and fluid inclusion study. Contributions to Mineralogy and Petrology, 144, 457–472.

Thomas, R., Förster, H.-J., Rickers, K., and Webster, J. (2005) Formation of extremely F-rich hydrous melt fraction and hydrothermal fluids during differentiation of highly evolved tin-granite magmas: a melt/fluid-inclusion study. Contributions to Mineralogy and Petrology, 148, 582–601.

Thomas, R., Kamenetsky, D., and Davidson, P. (2006a) Laser Raman spectroscopic measurements of water in unexposed glass inclusions. American Mineralogist, 91, 467–470.

Thomas, R., Schmidt, C., Veksler, I., Davidson, P., and Beurlen, H. (2006b) The formation of peralkaline melt fractions: Evidence from melt and fluid inclusion studies. Estudos Geológicos, 16, 61–67.

Thomas, R., Webster, J.D., and Davidson, P. (2006c). Understanding pegmatite formation: The melt and fluid inclusion approach. Mineralogical Association of Canada Short Course, 36, 189–210.

Thomas, R., Webster, J.D., Rhede, D., Seifert, W., Rickers, K., Förster, H.-J., Heinrich, W., and Davidson, P. (2006d) The transition from peraluminous to peralkaline granitic melts: evidence from melt inclusions and accessory minerals. Lithos, 91, 137–149.

Tolédano, P. (1964) Contribution à l'étude des borates de potassium et de rubidium. Revue de Chimie minérale, 1, 353–413.

Touboul, M., Penin, N., and Nowogrocki, G. (2003) Borates: A survey of main trends concerning crystal-chemistry, polymorphism and dehydration process of alkaline and pseudo-alkaline borates. Solid State Sciences, 5, 1327–1342.

Von Dreele, R.B. (1997) Quantitative texture analysis by Rietveld refinement. Journal of Applied Crystallography, 30, 517–525.

MANUSCRIPT RECEIVED JUNE 27, 2007
MANUSCRIPT ACCEPTED JANUARY 15, 2008
MANUSCRIPT HANDLED BY EDWARD GREW